COMPUTER SCIENCE

Bayesian reconstruction of rapidly scanned mid-infrared optoacoustic signals enables fast, label-free chemical microscopy

Constantin Berger[1,2,3], Myeongseop Kim[1,3], Lukas Scheel-Platz[1,2,3,4], Andreas Eigenberger[5], Lukas Prantl[5], Panhang Liu[1,3], Vipul Gujrati[1,3], Vasilis Ntziachristos[1,3,6], Dominik Jüstel[1,2,3]*, Miguel A. Pleitez[1,3]*

Hyperspectral optoacoustic microscopy (OAM) enables obtaining images with label-free biomolecular contrast, offering excellent perspectives as a diagnostic tool to assess freshly excised and unprocessed biological samples. However, time-consuming raster scanning image formation currently limits the translation potential of OAM into the clinical setting, for instance, in intraoperative histopathological assessments, where micrographs of excised tissue need to be taken within a few minutes for fast clinical decision-making. Here, we present a non–data-driven computational framework tailored to enable fast OAM by rapid data acquisition and model-based image reconstruction, termed Bayesian raster-computed optoacoustic microscopy (BayROM). Unlike data-driven approaches, BayROM does not require training datasets, but instead, it uses probabilistic model-based reconstruction to facilitate fast high-resolution imaging. We show that BayROM enables acquiring micrographs 10 times faster on average than conventional raster scanning microscopy and provides sufficient image quality to facilitate the intraoperative histological assessment of processed fat grafts for autologous fat transfer.

INTRODUCTION

Intraoperative histopathological examinations are crucial for precise surgical decision-making, for instance, in tumor margin analysis (*1*). The clinically established workflow for histological assessment usually consists of immunohistochemical or hematoxylin and eosin stains applied to excised tissue samples, followed by an examination via bright-field microscopy (*2*). Tissue staining uncovers biomolecular features required for histopathological examinations, such as tumor margin assessments or quality guidance for autologous fat transfer. Autologous fat transfer is an innovative therapeutic procedure that is increasingly used in plastic and aesthetic medicine, primarily aimed at promoting tissue regeneration and restoring volume. In addition to its regenerative applications, this technique plays a crucial role in breast reconstruction following tumor removal, where transplanted autologous fat provides both aesthetic and functional benefits. Specially mechanically processed fat graft, called cell-enriched lipotransfer (CELT or CELT^{plus}), shows strong capabilities to improve tissue regeneration and rejuvenation (*3*). However, the enrichment process currently lacks an intraoperative imaging step that can provide histological metrics on the processed fat graft as a predictive marker for therapeutic success and to avoid complications. Conventional workflows for histological assessments are currently insufficient to analyze molecular and morphological compositions of freshly excised tissues in real-time due to the time-consuming and laborious preparation steps, which can delay or hinder surgical decision-making (*4*). In addition, while current fast histology techniques used in, for instance, intraoperative tumor margin assessment are rapid (~10 min), they often come with the risk of inaccuracies, as they lack the necessary molecular specificity of conventional histology examinations (*5*).

As an alternative to conventional histology, label-free optoacoustic microscopy (OAM) has been proposed as a method for rapid intraoperative histology due to its ability to obtain intrinsic molecular contrast that enables avoiding the tissue preparation steps usually required for exogenous staining (*6*, *7*). In particular, optoacoustic hyperspectral imaging, i.e., sequential imaging at multiple excitation wavelengths over a spectral range, is key for tissue classification based on spectral hallmarks. However, although label-free OAM for histological examination saves time in tissue preparation, acquiring optoacoustic micrographs is often more time consuming than routinely used bright-field microscopy as image formation in many OAM systems is achieved by point-by-point raster scanning. Although technologies for wide-field OAM were proposed to bypass the need for time-consuming raster scanning, these methods often suffer from poor spatial resolution and shallow imaging depth (*8*). Low imaging speed is one of the major limiting factors of OAM toward its implementation as an intraoperative histopathological assessment procedure, especially for hyperspectral imaging where time cost scales linearly with the number of excitation wave numbers acquired (*4*). Hyperspectral optoacoustic image formation with fast data acquisition, i.e., within a time range of a few minutes, is crucial to allow for faster surgical decision-making than conventional tissue staining methods (*9*).

To facilitate fast label-free OAM, several hardware-based methods have been developed, for instance, optoacoustic microtomography (*10*), which allows the acquisition of numerous wide-field image volumes per second. Nevertheless, optoacoustic microtomography

[1]Institute of Biological and Medical Imaging, Bioengineering Center, Helmholtz Zentrum München, Neuherberg, Germany. [2]Institute of Computational Biology, Bioengineering Center, Helmholtz Zentrum München, Neuherberg, Germany. [3]Chair of Biological Imaging, Central Institute for Translational Cancer Research (TranslaTUM), School of Medicine and Health and School of Computation, Information, and Technology, Technical University of Munich, Munich, Germany. [4]Ludwig Maximilian University of Munich, Munich, Germany. [5]Department of Plastic, Hand, and Reconstructive Surgery, University Medical Center Regensburg, Regensburg, Germany. [6]Munich Institute of Robotics and Machine Intelligence (MIRMI), Technical University of Munich, Munich, Germany.
*Corresponding author. Email: dominik.juestel@tum.de (D.J.); miguel.pleitez@tum.de (M.A.P.)

leads to complex optical forward problems, making image formation more prone to artifacts compared to OAM with single-spot illumination combined with raster scanning. Further hardware-based solutions include accelerated raster scanning by optical setups involving voice coil stages (*11*), microelectromechanical systems (*7*, *12*, *13*), polygonal mirror scanners (*14*), and galvanometer scanners (*15*). However, in the context of raster scanning OAM, hardware-based solutions cannot be applied without substantial limitations, such as imaging artifacts that originate, for instance, from narrow field-of-views (FOVs). Another common limitation of hardware-based strategies for accelerating imaging speed in OAM is the sensitivity variation caused by the misalignment of the excitation beam with the detection area of the ultrasound transducer typically used for OA detection. In particular, confocal alignment of the excitation laser beam with the transducer is of special relevance in mid-infrared (mid-IR) OAM and spectroscopy (*16*), where reflective objectives are preferred against diffractive optics to avoid achromatic aberration due to the wide spectral range detected (for instance, between 2850 and 1000 cm^{-1}). The use of reflective objectives in mid-IR OAM renders using, for instance, galvanometer scanning ineffective because of the narrow FOV that can be imaged at each location, requiring mosaicking techniques and postprocessing correction of the abovementioned transducer's sensitivity field and laser beam excitation misalignment (*17*). However, the optical and acoustic properties of mid-IR OAM in terms of signal-to-noise ratio (SNR), resolution, and the homogenous transducer sensitivity field are crucial for enabling the assessment of freshly excised and unprocessed biological samples. Hence, an alternative method for increased imaging speed of raster scanning OAM, which can overcome the limitations of existing hardware-based solutions, is required to advance the field of fast intraoperative histology.

A strategy to enhance imaging speed while maintaining the advantages of single-point raster scanning of OAM systems, such as mid-IR OAM, is the use of rapid raster scanning in combination with computational methods. Rapid raster scanning can be achieved by (i) sparse scanning, i.e., acquiring only a fraction of all pixel intensities, and (ii) low averaging of optoacoustic signals per pixel and consequently reconstructing full images based on sparse and noisy data. To reconstruct full images based on sparse data, i.e., compensate for the inherent information loss, data-driven methods involving machine learning (ML) and deep learning (DL) have been applied (*18*–*21*). ML and especially DL are effective tools in the realm of image processing and enhancement, including denoising (*22*–*25*). However, in learning-based methods, the model architectures often used operate as black-box models and do not provide the necessary transparency to ensure artifact-free images, particularly for out-of-distribution data, i.e., sample types that were not covered by the training data (*26*–*29*). To mitigate the risk of imaging artifacts for a broad range of sample types, data-driven methods would require large amounts of training data, which are often unavailable or impractical to collect in OAM. Thus, although data-driven computational methods have shown promising capabilities for image reconstruction from incomplete data, they cannot ensure artifact-free images for a broad range of sample types due to the lack of big training data in OAM. An alternative to data-driven methods includes, for instance, compressed sensing techniques, where prior information about the sample is integrated via sparsity assumptions (*30*, *31*). Compressed sensing has, for example, been used in the realm of electron microscopy to reduce electron doses by sparse imaging (*32*, *33*). Another non–data-driven method that has been established for electron microscopy is beta process factor analysis (BPFA) (*34*). BPFA is a dictionary-learning method that can, for instance, be used for image reconstruction from sparse data. Dictionary-learning methods constitute a group of techniques that have furthermore been used for image denoising without requiring noise estimates (*35*). Because of a lack of accuracy combined with the high computational time required for dictionary-learning approaches, further methods, including regularized least-squares image reconstruction, were proposed (*36*). However, neither regularized least-squares methods, dictionary-learning, nor compressed sensing methods usually provide parameters for uncertainty quantification and, thus, similarly to data-driven methods, cannot deliver a quality assessment for reconstructed images to ensure artifact-free imaging. Furthermore, the previously summarized methods address either image reconstruction from sparsely sampled data or image denoising but mostly do not target both at the same time. Hence, a transparent alternative for computational reconstruction and denoising for rapid raster-scanned OAM data, including a quality-check readout, is required to push the boundaries of label-free imaging toward its integration into intraoperative workflows.

We hypothesized that by implementing rapid data acquisition in combination with model-based image reconstruction, we could accelerate the imaging speed of OAM over conventional raster scanning. In addition, by applying model-based image reconstruction, we could circumvent the limitations imposed for learning-based methods, i.e., the need for big data and/or the nontransparency of neural networks. For this purpose, we developed a computational imaging method termed Bayesian raster-computed optoacoustic microscopy (BayROM). BayROM facilitates the reconstruction of images based on rapid and thus incomplete raster scanning data, while not being required to train a model, and thus bypasses the need for large amounts of training data in OAM. Instead of implicitly learning priors via a dataset, BayROM uses an explicit prior model resembling knowledge about the imaged specimen. To maintain similar image quality as in full raster scanning, BayROM reconstructs images after rapid data acquisition supported by a parameterizable model, including optomechanical system properties by means of variational Bayes, and thereby achieves a 10-fold increase in imaging speed compared to conventional raster scanning in OAM.

Here, we showcase BayROM in the context of fast label-free biomolecular imaging by mid-IR hyperspectral microscopy, demonstrating its capability to reduce imaging time from the timescale of hours to only a few minutes. We validated BayROM's ability for fast tissue imaging on several mouse organ tissues as well as synthetic phantoms. Moreover, to demonstrate the use of BayROM for clinical practice, we investigated its capability to assess fresh fat grafts for autologous fat transfer, where a fast molecular imaging modality could substantially contribute to further improving treatment outcomes and reducing the need for follow-up surgeries. Here, we show that BayROM can provide high-resolution molecular images within only a few minutes, enabling the differentiation between $CELT^{plus}$ and nanofat. Nanofat is an enhanced fat graft with insufficiently removed released lipids that can cause complications, including oil cysts (*37*). While conventional histology methods fail to provide such assessment of fat grafts intraoperatively, we demonstrate the potential of BayROM for intraoperative decision-making in plastic surgery to potentially improve therapeutic responses and avoid complications and consequent follow-up surgeries.

RESULTS

Working principle of BayROM

Figure 1 graphically illustrates the working principle of BayROM as compared to conventional raster scanning in OAM. Raster scanning OAM measures the optoacoustic signal intensity in each pixel location to compose an image. BayROM increases imaging speed in OAM by systematically skipping raster scanning lines during optoacoustic signal acquisition and compensates for the missing information using Bayesian image reconstruction. Therein, a prior model constrains the reconstruction of unscanned areas to plausible values based on the scanned areas. Our knowledge of the measurement process (encoded in the forward model) and the measurement noise allows us to calculate to what degree a candidate image is compatible with the observed data. Furthermore, a priori knowledge about the imaged specimen is included in the form of a generative prior model, which statistically describes the structural properties of images in the harmonic/Fourier domain (see Materials and Methods). On the basis of the prior model and likelihood, we can express the

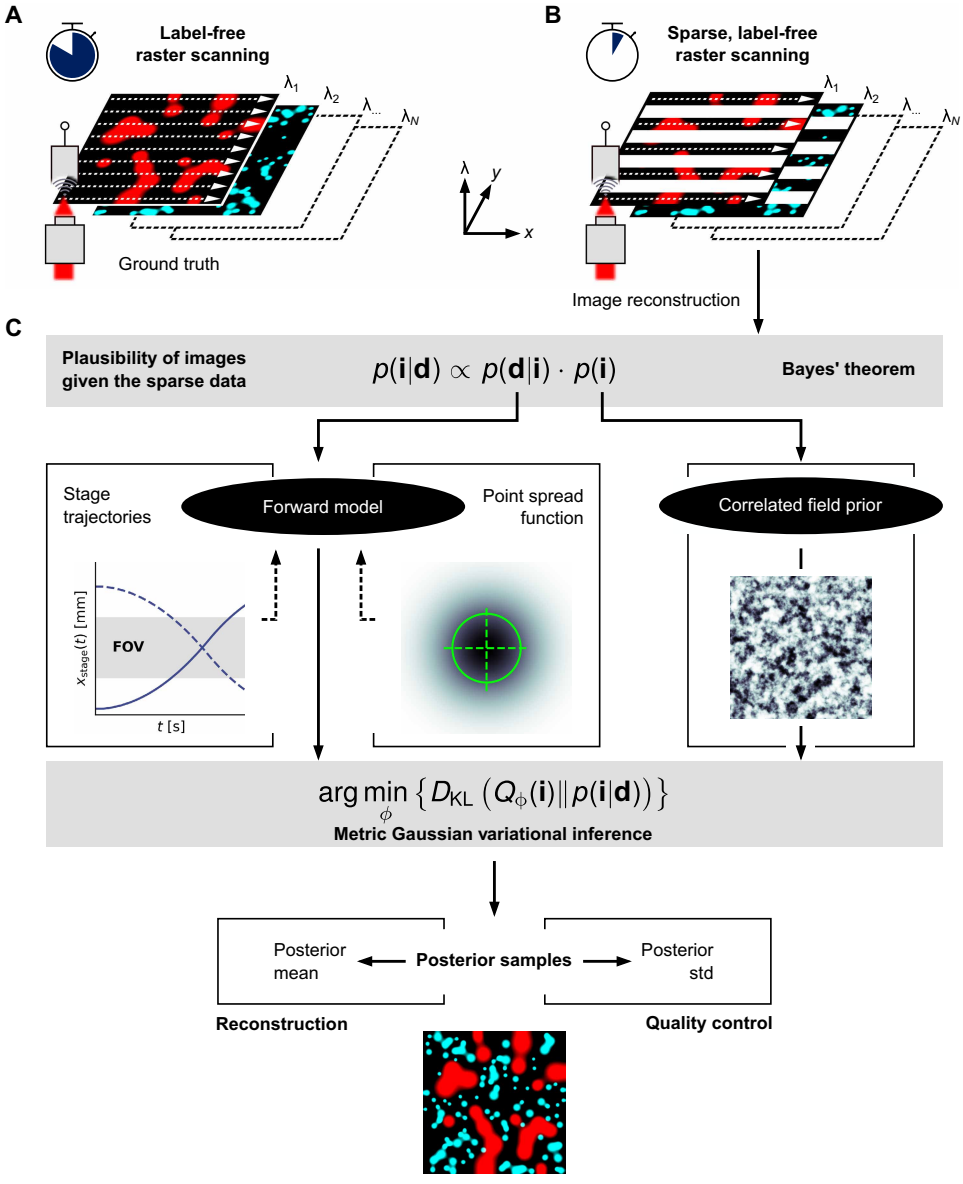

Fig. 1. Fast label-free imaging using rapid raster scanning and Bayesian image reconstruction. (**A**) OAM workflow. Raster-scanning OAM enables label-free imaging of unprocessed, freshly excised tissue samples. However, raster scanning is a tedious procedure that prevents fast intraoperative decision-making due to time-consuming data acquisition. (**B**) Workflow of Bayesian raster computed optoacoustic microscopy (BayROM). Rapid raster scanning can be applied to decrease the data acquisition time by a factor of 10. Image reconstruction is required to obtain high-resolution micrographs based on the compressed data. (**C**) Image reconstruction workflow. The probabilistic reconstruction framework creates plausible images given the reduced but rapidly acquired data. The plausibility of image candidates can be assessed using the Bayesian posterior probability $p(\mathbf{i}|\mathbf{d})$, which is proportional to the product between the likelihood $p(\mathbf{d}|\mathbf{i})$ and the prior $p(\mathbf{i})$. The likelihood evaluates the compatibility of image candidates with observed data given by the forward model. The prior model (correlated field prior) compensates for the information loss due to rapid scanning. The mean of the posterior approximated using MGVI serves as the reconstructed image, while the approximated posterior variance provides a metric for quality control.

plausibility of an image given the acquired data using Bayes' theorem. Bayes' theorem allows assigning a plausibility score (posterior probability) from 0 (the image is incompatible with the data, prior knowledge, or both) to 1 (only this image is compatible with the prior knowledge and the observed data). On the basis of the mean and standard deviation of the posterior probability distribution, we can generate image reconstructions, including pixel-wise uncertainty estimates. We approximate the posterior distribution using the metric Gaussian variational inference (MGVI) algorithm (*38*), which generates a set of posterior samples. We subsequently calculate posterior means and standard deviations based on the posterior samples. The reconstructed image is derived from the posterior mean, while the posterior standard deviation gives a lower bound of the pixel-wise uncertainty in the reconstruction, which can be used to obtain a quality control metric of reconstructed images. More details on the theoretic principle of BayROM are given in Materials and Methods. Uncertainty-based quality control facilitates the evaluation of reconstructions without the need to compare to a usually unavailable ground truth (GT) measurement. Therefore, we use the mean relative standard deviation (MRSD) of the posterior distribution as a metric to reflect the reconstruction uncertainty. Using the MRSD, our Bayesian imaging framework allows for quality-controlled image reconstruction based on rapid raster scanning to enable fast optoacoustic imaging.

Imaging characterization and evaluation in synthetic samples

First, we characterized BayROM's accuracy by comparing BayROM reconstructed micrographs of a synthetic test target (carbon tape; see Materials and Methods for details) with full raster scanning images, used as GT, of the same sample. Figure 2A shows GT and corresponding BayROM reconstructed micrographs (2 mm–by–2 mm FOV and 5-μm pixel size) for the test target at 2850 cm^{-1} excitation. While full raster scanning (GT) required 23.43 min for acquisition, data acquisition with 92.5% data reduction, i.e., only 7.5% of the amount of data needed for full raster scanning, required only 2.15 min, thus achieving an ~10-fold speedup with an excellent reconstruction accuracy as determined by a structural similarity index measure (SSIM) of 0.978 between GT and BayROM reconstructed micrographs. Figure 2A brings more details on the reconstruction results, including a back projection image shown to visualize the usable information contained in the rapidly acquired data (see Fig. 2B). Furthermore, Fig. 2A exhibits the posterior distribution represented by the posterior samples, posterior mean, and posterior standard deviation. The pattern of the posterior standard deviation follows the sample structure, which reflects localization uncertainties related to the point spread function (PSF). Such localization uncertainties can mainly be found at sharp intensity edges since the PSF leads to smoothed scanning data that represent such edges and thus cause uncertainties in their reconstruction. In addition to quantitative assessment of the reconstruction accuracy using the SSIM, Fig. 2C exhibits a qualitative comparison using overlay and cross-sectional intensity plots with no noticeable deviations, confirming accurate reconstruction. Figure 2D shows that the reconstruction intensities (i.e., the values of the micrograph after reconstruction) cover the full dynamic range of the GT and follow an almost linear power-law relationship with the GT values, which is important for quantitative imaging where contrast levels in a micrograph indicate optical absorption of the sample at a given wave number. Furthermore, Fig. 2E visualizes the distribution of the pixel-wise relative standard deviation (RSD), i.e., the ratios between the posterior standard deviation and the posterior mean for all pixels in the image. The overall uncertainty given by the MRSD amounts to 4.7% and thus indicates high confidence in the algorithm to reconstruct the images.

Next, we studied the effects of varying data reduction parameters on the reconstruction quality to determine a suitable configuration for optimal image quality and imaging speedup. The data reduction is mainly determined by the sparsity parameter, which describes how many raster lines are skipped to increase the data acquisition speed. The data acquisition speed scales linearly with the level of sparsity, i.e., if half of the raster lines are being skipped, then data acquisition will be twice as fast. To generate the results shown in Fig. 2 (A to E), we skipped three of four raster lines compared to full scanning, i.e., 75% sparsity. With the given sparsity levels, the distances between the raster lines remain smaller than the imaged structures, such that the relevant structural information of the imaged sample is still captured while the scanning speed is increased. The sparsity of 75% leads to an overall data reduction of 92.5%, since, in addition to sparsity, we decreased the averaging level per pixel compared to full raster scanning. High averaging per pixel causes slow stage movements along the imaged raster lines, and, thus, we decreased the averaging level so that the stage could operate at maximum speed. To study the effects of changing the number of skipped lines, we analyzed sparsity levels of 50% (every second raster line imaged), 75% (every fourth raster line imaged), and 87.5% (every eighth line skipped), which lead to overall data reduction levels of 85%, 92.5%, and 96.6%. The speedup resulting from the rapid data acquisition depends on the level of data reduction and increases with increasing data reduction. At the same time, image quality decreases with increasing data reduction levels. We compared the reconstruction qualities corresponding to data reduction levels of 85%, 92.5%, and 96.6%, leading to acquisition speedup factors of ~5, 10, and 20, respectively. Figure 2F visualizes the error distributions of the reconstructions, referring to the pixel-wise absolute errors between reconstructions and GT, corresponding to each data reduction level. The analysis of the reconstruction error distribution with respect to the data reduction level shows that the mean reconstruction error remains similar between the compared data reduction levels. However, the maximum reconstruction errors increase notably with increasing data reduction. In general, the choice of a data reduction level and, thus, the resulting speedup constitutes a trade-off in image quality and imaging speed that strongly depends on the application and thus needs to be seen as a parameter of BayROM and chosen accordingly. The results displayed in Fig. 2 demonstrate the capabilities of BayROM to accurately reconstruct images based on rapid data acquisition under consideration of varying data reduction parameters and inherent imaging speedups.

To further characterize the image enhancement capabilities of the reconstruction mechanism, we analyzed BayROM's resolution along with the SNR in reconstructed micrographs. Figure S1 (A to E) exhibits the estimated resolution of BayROM. It can be observed that the resolution of full raster scanning micrographs is, on average, 3.1 to 4.0 μm, while for BayROM, the estimated resolution is, on average, 4.5 to 5.6 μm. Furthermore, BayROM shows a lower resolution in the sparsely sampled axis, as indicated by the high variance of resolution estimates compared to the densely sampled axis. BayROM's overall resolution is 0.5 to 2.5 μm lower than full raster scanning because of the regularization effect of the reconstruction

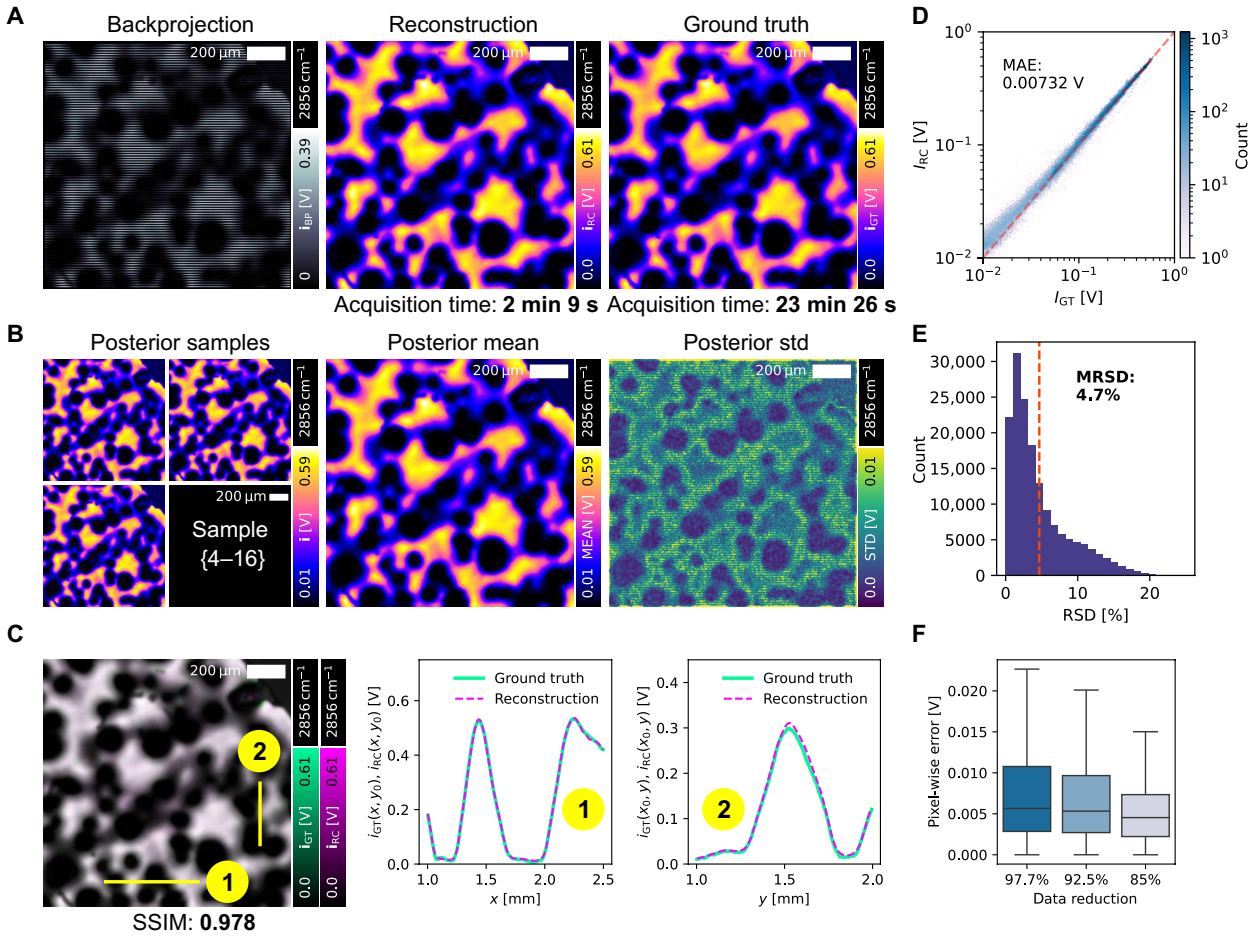

Fig. 2. Reconstruction analysis and characterization on a test phantom. (**A**) Visual comparison of back-projected data (BP), reconstruction (RC), and ground truth (GT). The back projection shows a horizontal line pattern, which originates from the data reduction. The SSIM between reconstruction and GT is 0.978, while the root mean square error (RMSE) and the peak signal-to-noise ratio (PSNR) between GT and reconstruction are 10.21 µV and 19.91 dB, respectively. (**B**) Visualization of the posterior distribution. The posterior mean and variance are obtained based on a pixel-wise assessment of the posterior samples. The posterior standard deviation shows a horizontal line pattern, which reflects higher uncertainties in skipped lines due to the sparse data acquisition and increased uncertainty on the boundaries of tissue structures due to PSF-related localization uncertainty. (**C**) Overlay of reconstruction and GT. The overlay as well as the cross-sectional line plots in both the *x* and *y* directions confirm an almost perfect reconstruction of the GT. (**D**) Intensity comparison between reconstruction and GT. The distribution of intensities in the GT image versus the reconstructed image is well aligned on the centerline, meaning that there is negligibly low bias in the intensity profile of the reconstruction. MAE, mean absolute error. (**E**) Histogram of the pixel-wise RSD. The MRSD suggests an average reconstruction uncertainty of 4.7%. (**F**) Data reduction analysis. A change in the level of data reduction results in a similar mean of the pixel-wise error between reconstruction and GT. However, the error distribution gets expanded, as indicated by the bars. An overall data reduction level of 92.5% was used to generate the results shown in (A) to (E).

mechanism. Although regularization causes a slightly decreased resolution, it enables denoising the reduced scanning data, i.e., maintains high SNR in the reconstructions despite noisy data due to rapid scanning. To demonstrate the denoising capabilities of BayROM, we analyzed the SNR of optoacoustic signals before and after image reconstruction. Figure S1 (F and G) shows that BayROM's data SNR, i.e., the SNR of the acquired optoacoustic intensities per pixel, is significantly lower, while its image SNR, i.e., the SNR of the pixel intensities after image reconstruction, is slightly higher than for the case of full raster scanning. With BayROM's image SNR of 53 compared to 48 for full raster scanning, we can confirm that BayROM not only maintains but also slightly increases the image SNR compared to full scanning despite substantially more noise due to less averaging per pixel. Although we confirmed that BayROM has only a slightly decreased resolution compared to full scanning and shows promising denoising capabilities, the analysis could potentially differ when being examined under different conditions, i.e., different data reduction settings, a larger FOV, or a more heterogeneous sample.

Fast hyperspectral imaging of unprocessed white adipose tissue

To demonstrate the capabilities of BayROM for fast imaging of biological specimens, we assessed the imaging speed as well as the reconstruction accuracy of images obtained for white adipose tissue (WAT) excised from mice at multiple excitation wave numbers (i.e., at multiple contrast channels). Specifically, we imaged fixed epididymal WAT taken from Friend leukemia virus B mice for an FOV of 1 mm

by 1 mm and a pixel size of 2.5 μm at selected wave numbers, including 2856 and 1550 cm^{-1}, which provide mainly contrast for lipids and proteins, respectively. Figure 3 (A to F) shows more details about the imaging performance, including an overlay of the reconstructions for each channel compared with the corresponding GTs. Figure 3C shows cross-sectional intensity plots of the GT and reconstructed image in both the x and y directions, demonstrating accurate reconstruction. Figure 3D shows the GT and reconstruction intensity values of all excitation wave numbers in a scatterplot, indicating no noticeable biases, thus suggesting linear behavior between GT and reconstructed pixel intensities in the entire value range. For an overall data reduction of 92.5%, i.e., three of four raster lines skipped, BayROM achieves ~10 times faster data acquisition while maintaining high image quality expressed by an SSIM of 0.950 by comparison with the GT. Similar to the characterization based on the carbon sample, we analyzed different data reduction levels, i.e., 85%, 92.5%, and 96.6%, to assess their corresponding performances. Figure 3 (E and F) shows reconstructed hyperspectral images of gonadal WAT imaged in an FOV of 1 mm by 1 mm with a pixel size of 2.5 μm. While all data reduction levels lead to SSIMs above 0.8, the data reduction of 96.6% shows that the structures of the adipocytes are becoming less recognizable in some parts of the image (SSIM of 0.805). While the 85% data reduction results in the highest SSIM value of 0.950, only a speedup factor of ~5 was achieved. Thus, imaging at a data reduction level of 92.5% offers, with a speedup factor of ~10 and an SSIM of 0.934, the best compromise between imaging speed and minimal deviations from GT. In this way, BayROM imaging enables higher information throughputs than full raster scanning, i.e., imaging more channels over time and thus facilitating fast hyperspectral imaging, i.e., the sequential image acquisition at different excitation wave numbers, which is specifically relevant to assess the biomolecular composition of imaged specimens.

Having achieved the ability to acquire images 10 times faster than with conventional raster scanning, we applied BayROM for hyperspectral imaging. This was demonstrated by sequential raster-scanning a WAT sample for an FOV of 1 mm by 1 mm and 5-μm pixel size at 80 different excitation wave numbers in two spectral ranges covering lipid (2800 to 2925 cm^{-1}) and protein contrast (1500 to 1700 cm^{-1}). On the basis of an overall data reduction level of 92.5%, we reconstructed each channel to compose an image stack. In fig. S2 (A and B), we visualized the GT image of WAT acquired by full faster scanning based on two channels (2856 and 1550 cm^{-1}) as well as the corresponding 80-channel BayROM image stack, denoted as hypercube. The hypercube contains the complete spatial and spectral information of the sample, i.e., each pixel on the hypercube comprises the mid-IR spectrum for the corresponding location in the sample. The spectral stability of hypercubes generated using BayROM, i.e., the accuracy of reconstructed spectra obtained from rapidly acquired data, was assessed by comparing the spectra obtained with the reconstructed hypercube at selected pixels with the GT spectra acquired from the same locations. We visualized the spectra from the BayROM hypercube in comparison with the GT spectra in fig. S2 (D to G), confirming that BayROM achieves accurate reconstructions of spectra, quantified by the mean relative error, which amounts to 4.4% for the adipocyte spectra and 1.7% for the extracellular matrix (ECM) spectra. To further analyze the imaged tissue, we used the GT spectra taken from the locations marked in fig. S2A representing adipocytes and ECM and performed linear spectral unmixing to generate a spatial mapping of the resulting mixing coefficients visualized in fig. S2C. The spatial mapping of unmixing coefficients can be used to assess the biological composition of the imaged sample, which, according to the unmixing, consists of 66.4% adipocytes and 33.6% ECM. In summary, we confirmed the hyperspectral imaging capability of BayROM, which is crucial for analytic downstream tasks, i.e., methods for data analysis applied after imaging, such as biological assessments based on spectral unmixing.

Validation of generalization based on mouse organ tissues

To analyze and validate the capabilities of BayROM on a broad range of biologically relevant sample types, we measured fixed tissues from several mouse organs. Specifically, we compared GT images obtained using full raster scanning with BayROM images based on two wave numbers, i.e., 2856 and 1550 cm^{-1}, to assess the lipid and protein contrast of the samples. Figure 3 (G to J) shows the results of muscle, pancreatic, liver, and kidney tissue scans. To prove the generalizability of BayROM, we demonstrate images of a 5 mm–by–5 mm FOV (large FOV) as well as a 1 mm–by–1 mm FOV (small FOV) for the muscle tissue and pancreatic tissue samples to showcase BayROM's application to particular structures in different scales. Furthermore, the same correlated field parameters were used to obtain the results displayed in Fig. 3 (G to J), i.e., the same parametrization was used for all images to confirm that BayROM is able to generalize to various sample types without parameter tuning. With average SSIM values ranging from 0.81 to 0.94 and total speedup factors ranging from 8.2 to 12.86, the results indicate that BayROM has the ability to successfully image various biological features, including connective tissue and adipocytes in the pancreatic sample, fiber structure in the muscle sample, and vessel structure in the liver sample. In summary, the presented results provide valuable insights into the generalizability and confirm that BayROM has substantial capabilities to reconstruct high-resolution images for arbitrary sample types while substantially increasing the imaging speed compared to full raster scanning.

Optoacoustic quality guidance for autologous fat transfer using BayROM

Having confirmed that BayROM enables fast, high-resolution molecular imaging of biological specimens, we assessed its capabilities to provide histological quality metrics for autologous fat transfer. Autologous fat transfer substantially enhances the overall quality of life for patients by aiding in the restoration of natural breast contour and improving tissue quality. Furthermore, autologous fat transfer is effectively applied in the treatment of conditions such as scar contracture, systemic sclerosis, and chronic wound healing (*39*, *40*). The principle of autologous fat transfer consists of the accumulation of stromal vascular cells, particularly adipose-derived stem cells, and ECM components using an intraoperative enrichment process to reduce the lipid content from depot adipocytes in lipoaspirate.

We applied BayROM to fresh, mechanically processed fat grafts aiming to establish quantitative quality control for autologous fat transfer. Figure 4 shows a representative example (from $n = 3$ independent measurements with similar results, as shown in fig. S3) comparing $CELT^{plus}$ and nanofat micrographs obtained by BayROM as well as full scanning. $CELT^{plus}$ is an enhanced fat graft obtained by mechanical processing of lipoaspirate to avoid nanofat transfer, which provides the risk of complications such as, for instance, oil

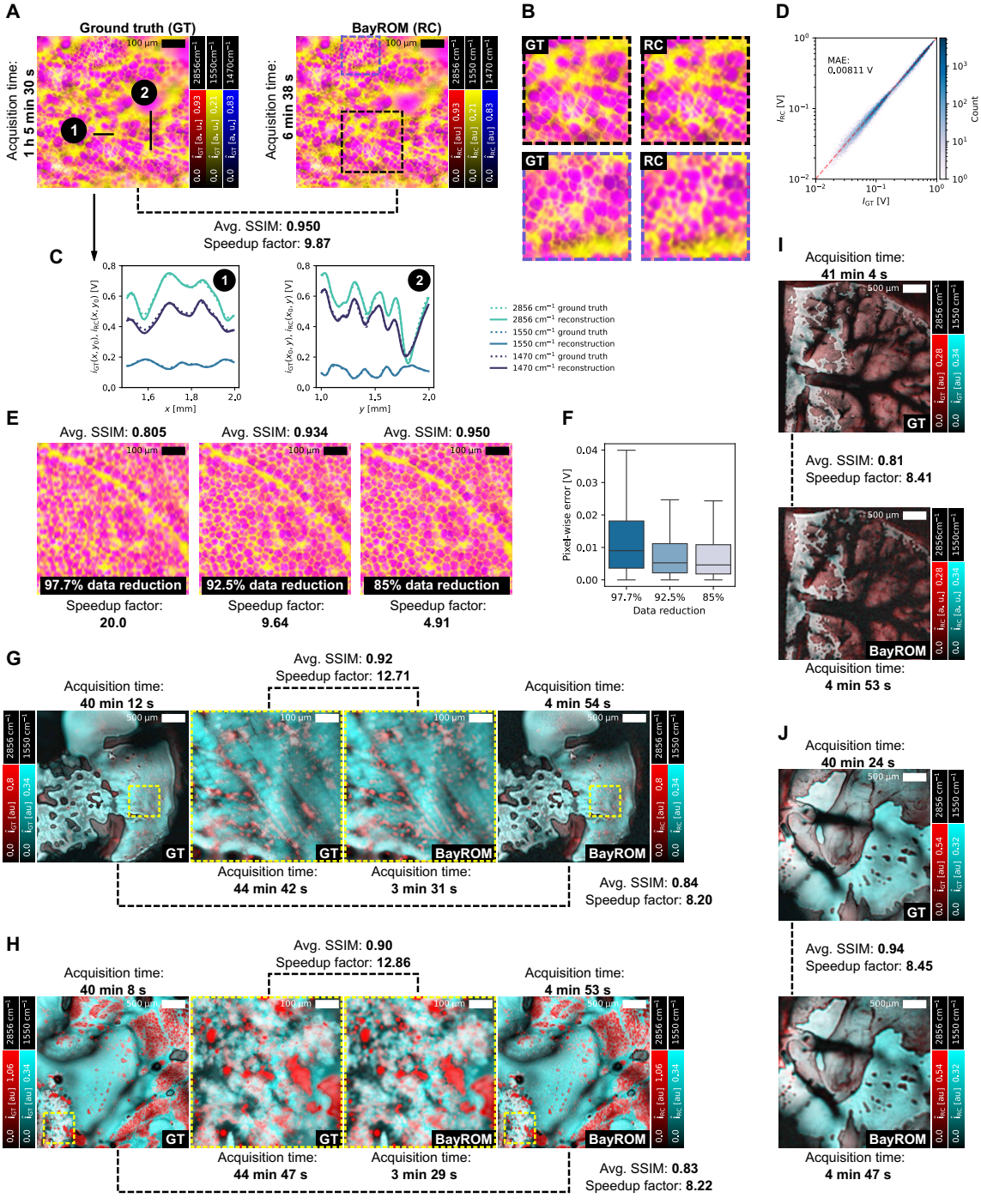

Fig. 3. Validation of BayROM based on biological samples. (**A**) Comparison of hyperspectral images of WAT using full raster scanning (GT) and BayROM (RC). The average RMSE and the average PSNR between GT and BayROM are 12.44 μV and 35.1 dB. au, arbitrary unit; h, hours. (**B**) Comparison of zoomed-in areas between GT and BayROM. (**C**) Comparison of reconstruction and GT using cross-sectional intensity plots in the *x* and *y* directions for each excitation wave number. (**D**) Quantitative comparison of reconstruction and GT with indicated MAE. (**E**) Comparison of data reduction levels. A data reduction level of 92.5% enables high reconstruction quality and ~10 times faster data acquisition. (**F**) Comparison of pixel-wise errors for data reduction levels shown in (E). (**G** and **H**) Image comparisons of large FOVs, i.e., 5 mm by 5 mm, and small FOVs, i.e., 1 mm by 1 mm, of mouse muscle, and pancreatic tissues imaged using full raster scanning (GT) and BayROM (92.5% data reduction). For the muscle tissue scans, the average RMSE and PSNR between GT and BayROM are 11.91 μV and 32.96 dB for the large FOVs, and 6.836 μV and 34.04 dB for the small FOVs. For the pancreatic tissue scans, the average RMSE and the average PSNR between GT and BayROM are 34.42 μV and 28.12 dB for the large FOVs, and 15.79 μV and 33.02 dB for the small FOVs. (**I** and **J**) Image comparisons of large FOVs, i.e., 5 mm by 5 mm, of mouse liver and kidney tissues imaged using full raster scanning (GT) and BayROM. For the liver tissue scans, the average RMSE and the average PSNR between GT and BayROM are 8.304 μV and 31.24 dB. For the kidney tissue scans, the average RMSE and the average PSNR between GT and BayROM are 5.853 μV and 36.89 dB.

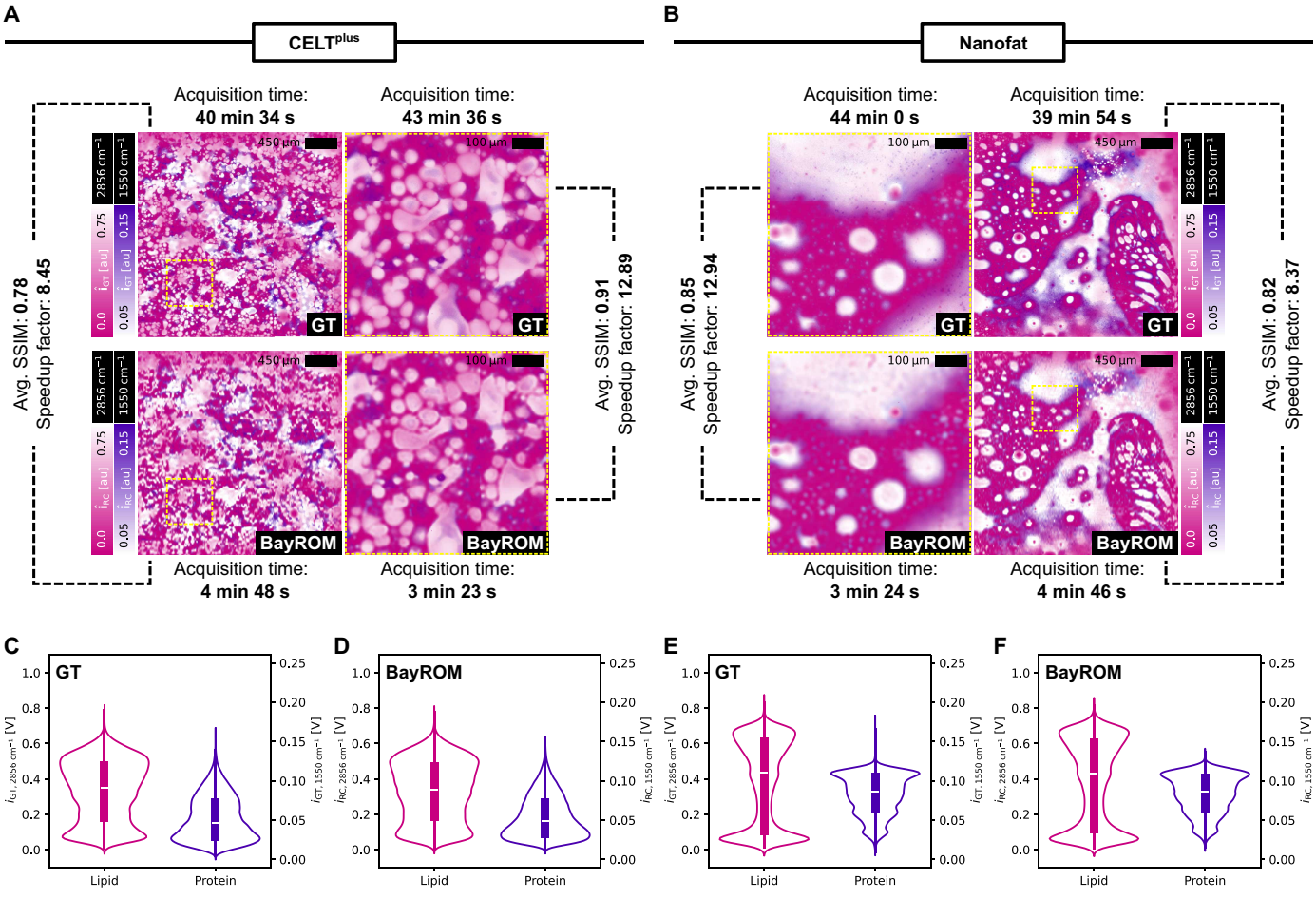

Fig. 4. Optoacoustic quality guidance of autologous fat transfer using BayROM. (**A**) Image comparisons of large FOVs, i.e., 4.5 mm by 4.5 mm (left column), and small FOVs, i.e., 1 mm by 1 mm (right column), of CELT^{plus} imaged using full raster scanning (GT) and BayROM (92.5% data reduction). The average RMSE and the average PSNR between GT and BayROM are 39.28 μV and 22.63 dB for the FOVs, and 13.27 μV and 31.04 dB for the small FOVs. (**B**) Image comparisons of large FOVs, i.e., 4.5 mm by 4.5 mm (left column), and small FOVs, i.e., 1 mm by 1 mm (right column), of nanofat imaged using full raster scanning (GT) and BayROM. The RMSE and the average PSNR between GT and BayROM are 34.15 μV and 26.67 dB for the large FOVs, and 11.25 μV and 32.62 dB for the small FOVs. (**C** and **D**) Intensity distributions of lipid and protein signals in large FOV images of CELT^{plus} obtained using full raster scanning (GT) and BayROM. (**E** and **F**) Intensity distributions of lipid and protein signals in large FOV images of nanofat obtained using full raster scanning (GT) and BayROM.

cysts due to insufficiently removed released lipids. Although the mechanical processing for CELT^{plus} aims to remove released lipids largely, the intraoperative enhancement protocol can only be standardized to a limited extent and thus can lead to insufficient removal of impurities and free lipids, i.e., nanofat. High-quality enhancement of fat grafts is required for treatment success and can only be confirmed via histological assessments. Figure 4 (A and B) shows micrographs at 2856 and 1550 cm^{-1} selected to assess the lipid and protein contrasts of CELT^{plus} and nanofat, respectively. The images were first obtained for a large FOV to reduce selection bias. From the large FOV, a zoomed image at a smaller FOV is obtained to further analyze small structures in more detail. BayROM achieves an increase of more than an eight times in imaging speed for the large FOVs and an increase of almost 14 times for the small FOVs compared to full raster scanning, resulting in a scanning time of 3 to 5 min per image.

As evident from Fig. 4 (A and B), both the BayROM images and the full scans of CELT^{plus} show highly compacted structures, including homogeneously distributed adipocytes, identifiable by their univacuolar lipid droplets, which are strongly embedded in the ECM. These adipocytes tend to be smaller than those typically found in adipose tissue depots. In contrast to CELT^{plus}, nanofat exhibits a notable presence of free lipids beside less prominent regions containing ECM and adipocytes. The free lipids present in nanofat could not be removed during the mechanical enrichment process. Besides the morphological differences between CELT^{plus} and nanofat, the images furthermore allow assessing the intensity distributions of both channels, which gives additional insights into the molecular compositions of both samples. Figure 4 (C to F) shows that the distributions calculated based on the BayROM images match the GT distributions. Comparing lipid and protein intensity distributions between CELT^{plus} and nanofat, the protein channel shows distinctly higher signals for nanofat than for CELT^{plus}. A predominately strong protein signal could indicate impurities caused by blood that are more present in nanofat than CELT^{plus}. Overall, the results suggest that BayROM enables a clear

morphological and molecular distinction between CELT^{plus} and nanofat based on the two-channel images and their corresponding intensity distributions. By providing fast, label-free images at imaging times below 5 min, BayROM could facilitate the quality assessment of mechanically processed fat grafts and thus enable interoperative decision-making for autologous fat transfer within a surgically reasonable time frame.

DISCUSSION

We showed that rapid data acquisition in OAM combined with Bayesian image reconstruction using BayROM leads to ~10 times faster imaging speed compared to full raster scanning while preserving image quality. Specifically, we validated BayROM based on synthetic samples and selected tissues from mouse organs that BayROM retains accurate reconstructions when compared to GT images acquired using full raster scanning. Raster scanning OAM is considered a low-throughput imaging technique due to its slow imaging speed. Slow imaging speed in OAM is a key limitation preventing its translation into clinical workflows despite its proven label-free molecular imaging capabilities. We demonstrated BayROM's translational potential for the case of autologous fat transfer, enabling rapid intraoperative histopathological assessment of fresh, unprocessed specimens. Thereby, BayROM achieves to overcome time-consuming image acquisition while avoiding limitations associated with hardware-based solutions, i.e., transducer defocusing, and bypassing the need for large datasets required by learning-based approaches that involve neural networks.

Model-based image reconstruction by BayROM is a non–data-driven approach that compensates for the data reduction using a generative prior model. Unlike learning-based approaches, BayROM does not require domain-specific training datasets to reliably compensate for missing information without the risk of generating artifacts. This main advantage of BayROM makes the tedious and often infeasible collection of large training datasets in OAM unnecessary. In addition, shifting from black-box DL-based reconstruction approaches to Bayesian image reconstruction offers more transparency by incorporating quality control parameters, i.e., the reconstruction uncertainty, for assessing the uncertainty associated with reconstruction results. However, image reconstruction with BayROM requires more computational effort/time than DL-based solutions. A high computational effort is required because model-based image reconstruction by BayROM is achieved using MGVI, a variational inference algorithm that solves a high-dimensional optimization problem. Contrary to data-driven DL-based solutions, where image reconstruction could be achieved by single forward propagation processes of neural networks, variational inference is solved in iterative loops. Nonetheless, fast image reconstruction using BayROM could be achieved by (i) increasing the computational power used for image reconstruction, (ii) optimizing hardware using graphics processing units for parallelized implementations of computational operations, etc., or (iii) approximate reconstruction, meaning that the posterior distribution is approximated with fewer iterations of the MGVI algorithm, making reconstructions faster than full reconstruction. To showcase the effects of approximate reconstruction, we analyzed the reconstruction accuracy for approximated versus full image reconstruction (fig. S4). To do this, we used three instead of five iterations of MGVI combined with eight instead of 16 samples drawn from the posterior distribution to reconstruct the images presented in Fig. 3 (A to F). Approximate reconstruction was carried out in only 2 min and 38 s compared to 10 min and 6 s needed for full reconstruction. The result shows that, even with approximate reconstruction, similar reconstruction residuals can be achieved compared to standard reconstruction while saving ~75% of the computational time. However, the maximum uncertainty in the approximate reconstruction is approximately twofold compared to the standard reconstruction method, which shows that the approximate solution provides less confidence about the resulting image than the full reconstruction and thus needs to be applied with the awareness that the imaging is potentially less accurate. In addition to approximate reconstruction, a potential strategy for accelerated computing could be realized by parallelizing the reconstruction of multiple image channels associated with different excitation wavelengths. When combining solutions 1, 2, and 3, we expect that the computational time required for image reconstruction using BayROM could be substantially lowered to obtain images within a few seconds instead of several minutes. While a hardware-efficient implementation is subject to further research to enable fast image reconstruction, the currently required computational time, which was necessary to assess the fat grafts presented in Fig. 4, is in the order of magnitude of 2 to 4 min per channel using approximate reconstruction. Hence, even without further developments, image reconstruction within a few minutes would currently delay but not hinder intraoperative decision-making using BayROM.

BayROM provides a parameterizable imaging framework that can be tuned to meet the specific needs of the application. The adjustable parameters include the data reduction setting, i.e., the number of skipped raster lines, as well as the pixel-wise averaging level, and define the imaging speed but also parameters referring to the reconstruction, such as the latent variables of the prior model (see Materials and Methods). However, since the correlated field model is tuned to act as a weakly informative prior, the appearance and quality of reconstructed images are not strongly influenced by the parameterization of the prior model. Instead, the reconstruction mechanism is rather affected by the correlation structure along the densely sampled axis, which gets projected to the sparsely sampled axis. Since most biological samples have similar correlation structures in all directions, such behavior aids highly resolved reconstruction without relying on a precise parameterization of the prior model for specific sample types. Benefiting from the ability to assess the correlation structure of images based on reduced data, we confirmed BayROM's capabilities to generalize to various sample types (see Fig. 3, G to J) without reparameterization.

Despite the generalization capabilities, the mechanism of capturing an overall correlation structure of images also provides the risk of artifacts, which is especially the case for images that express strongly differing correlation structures in different image areas. Figure S5 demonstrates two examples with blur and noisy artifacts resulting from different correlation structures expressed over the imaged FOV. Figure S5 (A and B) shows blurred fine structures, which can be the consequence of the reconstruction method capturing the dominant bulk areas and projecting their correlation structure also to areas with fine structures. Conversely, fig. S5 (C and D) shows an example where a bulk area in the BayROM image is noisier than the comparably smooth structure in the GT image. Such noisy bulk structures can be explained by the predominant correlation structures of small features in the images that are projected onto the bulk areas and make them appear as noisy. To avoid such

reconstruction artifacts, it is important to choose sparsity parameters such that the acquired data provide enough information about the structures of interest to enable their successful reconstruction. Hence, a thorough choice of parameters has to be made for data reduction levels to match the requirements of the clinical application and potential computational downstream analysis.

The overall benefit of our work is faster OAM imaging based on rapid data acquisition compared to conventional raster scanning OAM imaging. BayROM provides a parameterizable imaging framework that does not require the collection of training data, unlike related data-driven methods for image reconstruction based on reduced data. Furthermore, BayROM does not suffer from stitching artifacts in larger FOVs, such as common hardware-based solutions for fast scanning. A combination of optomechanical speedup methods with BayROM could potentially enable synergy between the hardware-based and software-based methods to further increase the data acquisition speed toward high-speed and high-throughput OAM applications. On the other hand, the overall limitation of BayROM is the high computational effort required for image reconstruction compared to DL methods. The next step is a hardware-optimized and parallelized implementation to be operated using more computational power to assess the imaging performance for clinical applications. An additional promising clinical application could be tumor margin segmentation based on fast hyperspectral imaging, which would be an important step toward the clinical implementation of BayROM with optimized computation.

In summary, we showed that BayROM, a rapid imaging method combined with a probabilistic image reconstruction algorithm, enables about 10 times faster data acquisition and accurate reconstructions, which we validated based on several mouse organ tissues. The impact of faster data acquisition is that increased scanning speed of raster scanning OAM by a factor of 10 could enable its integration into surgical workflows, such as quality guidance for autologous fat transfer. Although here, the application of BayROM for quality-guided autologous fat transfer was demonstrated only as a proof-of-concept, we were able to retrieve morphological and molecular differences between CELT^{plus} and nanofat. To move BayROM toward its clinical implementation, the next steps involve a clinical trial with a larger patient cohort to statistically investigate and validate the parameters retrieved for quality guidance of fat grafts. In conclusion, BayROM can facilitate the intraoperative histopathological assessment of freshly derived specimens showing great potential to enable fast surgical decision-making based on label-free molecular imaging.

MATERIALS AND METHODS

Molecular contrast formation and optomechanical setup

The ability of biological molecules to convert light to sound via the optoacoustic effect strongly depends on the arrangement and interaction of their constituent atoms and atomic bonds, as well as the wavelength of the light interacting with them. For this reason, biological molecules have characteristic optoacoustic spectral fingerprints, which OAM exploits to generate label-free molecular contrast. The types of molecules present in a sample, their spatial distribution, and local concentrations all shape a sample's ability to generate optoacoustic signals. OAM measures this position- and excitation wavelength–dependent optoacoustic signal generation ability, henceforth called the optoacoustic signal strength field $\mathrm{OASS}(x, \lambda)$. Molecular prevalences in tissues can be deduced by identifying molecular fingerprints in the optoacoustic signal strength field.

Mid-infrared optoacoustic microscopy (MiROM) (*16*), the OAM technique used in this work, uses a broadly tunable quantum cascade laser (MIRcat, Daylight Solutions) to probe the optoacoustic signal strength field of a sample with mid-IR radiation in the wave number range of 2941 to 909 cm^{-1} (3.4 to 11 μm). The sample is placed on a mid-IR transparent zinc sulfide window (Crystal) and illuminated from below. The laser beam is focused on a plane located in the imaged sample using a 0.5–numerical aperture reflective objective (36×; Newport Corporation) to confine the optical excitation to a small tissue volume. To sense the generated optoacoustic signal, we placed a focused ultrasound transducer (Imasonic) with a central frequency of 20 MHz above the tissue and coaligned to the focal spot of the mid-IR laser, capturing the optoacoustic signals through a coupling medium (deionized water). The optoacoustic signals are acquired using a data acquisition card (Gage Applied) after being amplified by a 63-dB low-noise amplifier (MITEQ) and processed by a 50-MHz low-pass filter (Mini-Circuits). The mid-IR laser has a repetition rate of 100 kHz and a pulse duration of 20 ns. Three exemplary wavelengths were used to assess the molecular response in investigated samples: 2856 cm^{-1} causing symmetric stretching of CH_2 functional groups, 1550 cm^{-1} causing N—H bending/C—N stretching, and 1470 cm^{-1} causing CH_2/CH_3 bending.

Raster scanning OAM maps the optoacoustic signal strength field by spatially raster-scanning the sample for each selected excitation wavelength. In each pixel location (indexed by the pixel coordinates $k \in \{1, \ldots, n\}$ and $l \in \{1, \ldots, m\}$), the optoacoustic signal strength field is probed with multiple laser pulses (indexed by the pulse number $j \in \{1, \ldots, 50\}$), yielding a set of optoacoustic transient signals $\mathrm{OAT}^{j}_{k,l}(t)$. These transient signals are subsequently averaged with respect to the laser pulses to increase the SNR, resulting in the averaged optoacoustic transient signal $\mathrm{OAT}_{k,l}(t)$. To form a MiROM micrograph

$$\mathbf{i}^* = \begin{pmatrix} i^*_{1,2} & \cdots & i^*_{1,m} \\ \vdots & \ddots & \vdots \\ i^*_{n,1} & \cdots & i^*_{n,m} \end{pmatrix} \tag{1}$$

with $n \cdot m$ pixels (henceforth called "image"), the peak-to-peak amplitudes of the averaged optoacoustic transient signals $\mathrm{OAT}_{k,l}(t)$ are extracted as the image pixel values

$$i^*_{k,l} = \max_t \left[\mathrm{OAT}_{k,l}(t)\right] - \min_t \left[\mathrm{OAT}_{k,l}(t)\right], \quad \forall k \in \{1, \ldots, n\}, l \in \{1, \ldots, m\} \tag{2}$$

We speed up data acquisition by skipping raster scanning lines l (sparsity) and reducing the number of optoacoustic transient signals acquired in each measurement location from 50 to 15 (decreased averaging). This acquisition approach yields reduced observations

$$\begin{aligned} d_{k,v} &= \max_t \left[\mathrm{OAT}'_{k,v}(t)\right] - \min_t \left[\mathrm{OAT}'_{k,v}(t)\right], \\ &\forall k \in \{1, \ldots, n\}, v \in \{1, w+1, 2\,w+1, \ldots\} \end{aligned} \tag{3}$$

where $\mathrm{OAT}'_{k,v}(t)$ denotes the averaged optoacoustic transient signals formed from 15 laser pulses, and w denotes the raster scanning line acquisition stride. When measuring every fourth raster scan line ($w = 4$), the amount of data acquired reduces by 92.5% with respect to a full scan.

The rapid measurements permit a substantial speedup of the data acquisition process but are realized at the cost of information loss with respect to the baseline. The increased stride between raster scanning lines creates areas in the micrograph where the optoacoustic signal strength field is not directly probed, and the reduction in repeated transient measurements leads to a reduced SNR in the data **d**. Consequently, reconstructing dense micrographs **i** based on the reduced data **d** is an ill-posed inverse problem (i.e., does not have a unique solution), which we address in the framework of Bayesian image reconstruction.

Exploitation of structural regularities in imaged samples

Many samples of interest for OAM have characteristic structural regularities, such as the grain structure of carbon tape or the arrangement, sizes, and shapes of adipocytes in WAT. The core concept of BayROM is that OAM images can be reconstructed faithfully from reduced data if the imaged samples exhibit structural regularities, which can be used to deduce the image values in areas without measurements from measurements in other areas. For example, knowledge of the typical shape and size of adipocytes in WATs allows predicting the full contour of a partially imaged adipocyte.

In general, i.e., for arbitrary samples, such structural regularities are not known a priori. Nevertheless, to reconstruct a broad range of samples, BayROM estimates the structural regularities of the imaged sample during the image reconstruction process based on the available data **d** and forms the image using the estimated regularities. For this purpose, we model the image as a (nonlinearly transformed) Gaussian random field with approximately Matérn covariance structure. The covariance structure encodes the structural regularities of the image and is inferred in the image reconstruction process. Although exploiting the structural regularities of the sample constrains the solution space, the imaging problem remains ill-posed.

Bayesian image reconstruction

Given that there is no unique solution to the image reconstruction problem, we pursue a probabilistic image reconstruction approach. We recover the discrete posterior probability distribution of images $p(\mathbf{i}\,|\,\mathbf{d})$, which expresses how likely it is that a full OAM scan would produce the image **i** given that a rapid scan has produced the data **d**. On the basis of the posterior distribution of images, we can estimate the expected image for a full OAM scan (via the posterior mean) and the uncertainty of this estimate (via the posterior variance).

Following Bayes' theorem, the posterior probability of an image **i** is proportional to the product of the so-called likelihood $p(\mathbf{d}|\mathbf{i})$ and prior probability distribution $p(\mathbf{i})$

$$p(\mathbf{i}|\mathbf{d}) \propto p(\mathbf{d}|\mathbf{i}) \cdot p(\mathbf{i}) \tag{4}$$

The likelihood encodes how probable it is to observe the data **d** for a sample that a full scan would produce the image **i**, given our knowledge about the measurement process. The prior probability distribution encodes our a priori knowledge about studied samples and their associated OAM images, such as the fact that the images are strictly positive-valued. We also encode our expectation that the images will have relevant structural regularities in the prior.

Computing posterior statistics given $p(\mathbf{i}|\mathbf{d})$ is challenging because of the high dimensionality of the images. We use variational inference to approximate the posterior distribution $p(\mathbf{i}|\mathbf{d})$ with a parametric distribution $Q_{\boldsymbol{\phi}}(\mathbf{i})$, which is constructed so that efficient computation of its distribution statistics becomes possible. The posterior mean and standard deviation can then be estimated using $Q_{\phi}(\mathbf{i})$. Variational inference approximates the true posterior distribution by minimizing the Kullback-Leibler (KL) divergence

$$D_{\mathrm{KL}}\left(Q_{\boldsymbol{\phi}} \| p\right) = \sum_{\mathbf{i}} Q_{\boldsymbol{\phi}}(\mathbf{i}) \log\left[\frac{Q_{\boldsymbol{\phi}}(\mathbf{i})}{p(\mathbf{i}|\mathbf{d})}\right] \tag{5}$$

between the posterior and the variational distribution $Q_{\boldsymbol{\phi}}(\mathbf{i})$. We use an algorithm optimized for high-dimensional spaces, MGVI (*38*), which represents the variational distribution $Q_{\boldsymbol{\phi}}(\mathbf{i})$ as a vector of latent samples $\boldsymbol{\phi} = \left(\boldsymbol{\psi}_1, \boldsymbol{\psi}_2, \ldots, \boldsymbol{\psi}_{n_{\mathrm{MGVI}}}\right)$. The image reconstruction process was implemented in the probabilistic inference framework Numerical Information Field Theory (NIFTy) (*41*, *42*) and was executed on an M2 MacBook Pro (Apple).

System forward model and likelihood definition

We model the measurement process of rapid OAM with the combination of a deterministic system response $R(\mathbf{i})$ and additive stochastic noise **n**

$$\mathbf{d} = R(\mathbf{i}) + \mathbf{n} \tag{6}$$

The deterministic system response includes, on the one hand, the effect of the PSF of the system and, on the other hand, the choice of measurement locations implied by the stage trajectories. The system PSF was characterized based on an image taken from a 1-μm (subresolution) polystyrene sphere (*16*). Numerically, the operator R is implemented as sequentially applying a PSF convolution operator R_{PSF} (which convolves the image **i** with a two-dimensional Gaussian kernel with a standard deviation of 5 μm in both spatial dimensions) and R_{stages}, which models the distribution of measurement locations and selectively copies values of the PSF-convolved image $\left(R_{\mathrm{PSF}}\,\mathbf{i}\right)_{k,l}$ to entries of the simulated data vector **d**. The additive noise **n** was characterized based on the dark noise of the system, which is measured by acquiring an image while blocking the quantum cascade laser beam and assessing the distribution of the pixel intensities. The dark noise was found to be independent and identically distributed Gaussian noise with a standard deviation of $\sigma = 9.318 \times 10^{-7}$ V. In summary, the rapid OAM measurement is modeled as

$$\mathbf{d} = R\mathbf{i} + \mathbf{n} = \left(R_{\mathrm{stages}} \circ R_{\mathrm{PSF}}\right)\mathbf{i} + \mathbf{n} \tag{7}$$

Accordingly, the likelihood $p(\mathbf{d}|\mathbf{i})$ is given by

$$p(\mathbf{d}|\mathbf{i}) = G\left[\mathbf{d} - R\mathbf{i}\,|\,\boldsymbol{\mu} = 0, \mathbf{N} = \sigma^2\mathbf{I}\right] \tag{8}$$

where G is a Gaussian distribution with mean $\boldsymbol{\mu} = 0$ and covariance $\mathbf{N} = \sigma^2\mathbf{I}$.

Image prior implementation

Following (*38*), we implement the image prior as a hierarchical generative model $\mathbf{i} = f(\boldsymbol{\psi})$, which deterministically transforms latent parameters $\boldsymbol{\psi}$ into images **i**. As stated in the "Exploitation of structural regularities in imaged samples" section, the images are modeled as a Gaussian random field GF with approximately Matérn covariance structure, which is nonlinearly transformed to model the strict positivity of OAM images

$$f(\boldsymbol{\psi}) = r \cdot \mathrm{sigmoid}\left[\mathrm{GF}\left(\boldsymbol{\psi}^{\mathrm{GF}}\right) + s(\boldsymbol{\psi}^{s})\right] \tag{9}$$

Here, r is a constant scaling factor setting the maximal obtainable image value. The sigmoid function ensures positivity of the generated images, while s is an additive offset that controls the average pixel value. The optimal additive offset for a given data vector $\mathbf{d}$ is inferred during reconstruction and a priori follows a Gaussian distribution with mean $\mu_s = 0.5$ and standard deviation $\sigma_s = 0.25$.

The Gaussian random field $\mathrm{GF}(\boldsymbol{\psi}^{\mathrm{GF}})$ is meant to capture and exploit the correlation structure of the image as described above. It is constructed via the Hartley amplitude field $\mathbf{A}(\boldsymbol{\psi}^{\mathrm{GF}})$, which is a harmonic representation similar to Fourier mode amplitudes based on the Hartley transform (HT)

$$\mathrm{GF}(\boldsymbol{\psi}^{\mathrm{GF}}) = \mathrm{HT}\left[\mathbf{A}(\boldsymbol{\psi}^{\mathrm{GF}})\right] \tag{10}$$

We model $\mathbf{A}$ as being separable into a length-scale dependent Hartley spectrum function $\mathrm{E}(|\mathbf{k}|)$ and a Gaussian random field $\boldsymbol{\psi}^{\boldsymbol{\xi}}$. Here, $\mathbf{k} = (k, l)$ is the wave vector indexing the Hartley modes. The Hartley spectrum function captures the smoothed spectral power distribution in $\mathbf{A}$, while the Gaussian random field $\boldsymbol{\psi}^{\boldsymbol{\xi}}$ captures deviations of the Hartley amplitudes $\mathbf{A}$ from E. Correspondingly, the Hartley amplitudes $\mathrm{A}_{k,l}$ is defined as

$$\mathrm{A}_{k,l} = \mathrm{E}_{k,l}\left(\psi^a, \psi^b, \psi^c\right) \cdot \psi^{\boldsymbol{\xi}}_{k,l} \tag{11}$$

$\mathrm{E}(|\mathbf{k}|)$ is constructed as a Matérn spectrum with learnable parameters $a(\psi^a)$, $b(\psi^b)$, and $\mathrm{c}(\psi^c)$

$$\mathrm{E}_{k,l} = a\left[1 + \left(\frac{\sqrt{k^2 + l^2}}{b}\right)^2\right]^{\frac{c}{4}} \tag{12}$$

This formulation of GF allows us to incorporate the a priori expectation of Matérn covariance for the image while permitting the reconstruction to produce images with covariance structures deviating from the Matérn form if the data suggest it. The priors for the Hartley spectrum function parameters a, b, and c are chosen as weakly informative to minimize the risk of biasing the reconstruction.

In summary, the hierarchical image model $f(\boldsymbol{\Phi})$ nonlinearly transforms latent parameter vectors $\boldsymbol{\psi} = \left(\boldsymbol{\psi}^{\boldsymbol{\xi}}, \psi^a, \psi^b, \psi^c, \psi^s\right)$ into images $\mathbf{i}$, which a priori exhibit Matérn covariance. Inserting $\mathbf{i} = f(\boldsymbol{\psi})$ into the measurement equation

$$\mathbf{d} = \mathbf{R}\mathbf{i}(\boldsymbol{\psi}) + \mathbf{n} = \left(\mathbf{R}_{\mathrm{stages}} \circ \mathbf{R}_{\mathrm{PSF}} \circ f\right)\boldsymbol{\psi} + \mathbf{n} \tag{13}$$

the image reconstruction problem can be reformulated as reconstructing the posterior distribution of the latent parameters $p(\boldsymbol{\psi}|\mathbf{d})$, which has practical benefits as outlined in (*43*).

Postprocessing

The outcome of the MGVI, i.e., a set of posterior samples $\phi = \left(\boldsymbol{\psi}_1, \boldsymbol{\psi}_2, \ldots, \boldsymbol{\psi}_{n_{\mathrm{MGVI}}}\right)$, is used to compute the posterior mean image $\mathbf{i}_{\mathrm{RC}}$

$$\mathbf{i}_{\mathrm{RC}} = \frac{1}{n_{\mathrm{MGVI}}} \sum_{i=1}^{n_{\mathrm{MGVI}}} f\left(\boldsymbol{\psi}_i\right) \tag{14}$$

$\mathbf{i}_{\mathrm{RC}}$ serves as reconstructed images after applying additional postprocessing steps. Postprocessing includes cropping the edges of the image, which were added to the reconstructed micrographs in the numerical convolution with the PSF. Furthermore, if needed, the reconstructed images are interpolated using linear interpolation to allow pixel-wise comparison of the reconstruction based on reduced data with the GT images. For visualization, contrast-limited adaptive histogram equalization (CLAHE) was applied to micrographs to emphasize image contrast. Images $\mathbf{i}$ that were processed with CLAHE are indicated as $\hat{\mathbf{i}}$. The reported computational times include the full image generation processes, i.e., reconstruction and postprocessing. However, the indicated imaging times do not include the computational time.

Uncertainty quantification

To quantify the overall uncertainty in reconstructed images, the MRSD was used. The MRSD is calculated based on the estimated posterior mean $i^{\mathrm{RC}}_{k,l}$ and standard deviation $u^{\mathrm{RC}}_{k,l}$ for each pixel

$$\mathrm{MRSD} = \frac{1}{m \cdot n} \sum_{k=1}^{n} \sum_{l=1}^{m} \frac{u^{\mathrm{RC}}_{k,l}}{i^{\mathrm{RC}}_{k,l}} \tag{15}$$

Since the MRSD expresses the average uncertainty relative to the reconstructed intensity values for the entire image, it can be used as a quality metric for reconstructed images without the comparison to a GT image.

Hyperspectral linear unmixing

For a demonstration of spectral unmixing based on the hypercube acquired using BayROM, linear unmixing was performed pixel-wise. Therefore, the spectra obtained using single-point optoacoustic spectroscopy were grouped into adipose tissue and ECM and averaged. The model for linear unmixing assumes that each pixel's spectrum is composed of a linear combination of both the adipose tissue and the ECM average spectrum. Therefore, the mixing coefficients were restricted to non-zero and determined using pixel-wise least-squares minimization. The result provides two coefficients for each pixel, which were mapped to the image using an overlay to visualize the unmixing result.

Evaluation metrics

The quantitative evaluation of BayROM is twofold. Because of the trade-off between the acquisition speed and the image quality, we report a speedup factor on the one hand and image quality metrics on the other hand. The speedup factor denotes the ratio between the data acquisition time of the full raster scans and the rapid scans. On the other hand, to quantify the image quality, i.e., the reconstruction accuracy, we report the SSIM, the root mean square error (RMSE), and the peak signal-to-noise ratio (PSNR) between the reconstructed images and the GTs. The SSIM is defined as

$$\mathrm{SSIM} = \frac{\left(2\mu_{\mathrm{RC}}\mu_{\mathrm{GT}} + c_1\right)\left(2\sigma_{\mathrm{RC,GT}} + c_2\right)}{\left(\mu^2_{\mathrm{RC}} + \mu^2_{\mathrm{GT}} + c1\right)\left(\sigma^2_{\mathrm{RC}} + \sigma^2_{\mathrm{GT}} + c_2\right)} \tag{16}$$

where μ_{RC} and μ_{GT} are the mean values of the reconstructed GT images, σ_{RC} and σ_{GT} are the variances of the reconstructed GT images, and $\sigma_{\mathrm{RC,GT}}$ is the covariance between reconstruction and GT. The variables $c_1 = 0.0001$ and $c_2 = 0.0009$ stabilize the division by small denominators. The RMSE error is defined as

$$\mathrm{RMSE} = \sqrt{\frac{1}{m \cdot n} \sum_{k=1}^{n} \sum_{l=1}^{m} \left(i^{\mathrm{GT}}_{k,l} - i^{\mathrm{RC}}_{k,l}\right)} \tag{17}$$

where $i_{k,l}^{GT}$ and $i_{k,l}^{RC}$ denote the intensity values of the GT image and the reconstruction for each pixel, respectively. The PSNR is defined as

$$\mathrm{PSNR} = 20 \cdot \log_{10}\left(\frac{i_{\max}}{\mathrm{RMSE}}\right) \tag{18}$$

where $i_{\max}$ denotes the maximum possible intensity value.

Signal-to-noise ratio

We used the SNR to characterize the data acquired using full raster scanning and rapid scanning. Thereby, we denote the SNR of unprocessed signals corresponding to a single pixel as data SNR. The data SNR is defined as

$$\mathrm{DSNR} = \frac{\mu_{k,l}}{\sigma_{k,l}} \tag{19}$$

where $\mu_{k,l}$ denotes the peak-to-peak amplitude of the averaged optoacoustic signal, and $\sigma_{k,l}$ is the standard deviation of the peak-to-peak amplitudes of each optoacoustic signal that is subject to be averaged and mapped to a pixel $\{k, l\}$. Furthermore, we reported the image SNR as the SNR in the image space, i.e., after image formation. Thereby, the image SNR is defined as

$$\mathrm{ISNR} = \frac{\mathrm{mean}\left(\tilde{\mathbf{i}}\right)}{\mathrm{std}\left(\tilde{\mathbf{i}}\right)} \tag{20}$$

where $\tilde{\mathbf{i}}$ is a selected subregion in an image $\mathbf{i}$ that is expected to have identical intensities. $\mathrm{mean}\left(\tilde{\mathbf{i}}\right)$ and $\mathrm{std}\left(\tilde{\mathbf{i}}\right)$ denote the mean intensity and the standard deviation of intensities in the subregion $\tilde{\mathbf{i}}$.

Resolution

To characterize BayROM's capabilities of precise image reconstruction, we computed resolution estimates based on the edge spread functions (ESFs) obtained from a synthetic sample with sharp intensity transitions. To obtain resolution estimates, we used the first derivative of a line profile perpendicular to a sharp intensity transition and defined the full width at half maximum of a Gaussian fit to the ESF as the resolution.

Animal tissue preparation

Male B6(Cg)-Tyr$^{c\text{-}2J}$/J mice were maintained under specific pathogen-free conditions with a 12-hour light/dark cycle at a controlled ambient temperature (20° to 24°C). Standard rodent chow and sterile-filtered water were provided ad libitum throughout the study. After 38 weeks of feeding, all mice were euthanized via intraperitoneal injection of 0.8-ml anesthetic cocktail (composition: 6 ml of NaCl, 1 ml of ketamine, and 0.25 ml of xylazine). After blood removal, muscle tissues, pancreatic tissues, liver tissues, and kidney tissues were excised and immediately fixed in 4% paraformaldehyde phosphate-buffered saline solution at room temperature for subsequent analyses. For BayROM imaging, tissue specimens were prepared as follows: The samples were placed in a custom-designed dish equipped with a 12.7-mm-diameter ZnSe window. Ultrasonic gel was uniformly applied to the tissue surface to avoid air bubbles and ensure sufficient sound coupling. The gel-covered tissue was sealed with polyethylene film, followed by the addition of D_2O as an optical coupling medium. All animal experiments were approved by the government of Upper Bavaria and carried out in accordance with the approved guidelines under the following file number: TV 55.2-2532.Vet_02-20-121.

Human fat graft preparation

Human lipoaspirate was obtained with informed patient consent and approval from the Ethics Committee of the University of Regensburg, Germany (24-3640-101, amendment number 24-3640_1-101). Discarded tissue from elective liposuction procedures was used for sample collection. The procedure was performed using water jet–assisted liposuction (body-jet evo, Human Med AG, Schwerin, Germany) as previously described (*3*), using a pulsatile jet of saline (0.9% NaCl containing epinephrine at 1:200,000) to gently dislodge adipose tissue. Suction peaks below 0.5 bar were avoided. Postharvest, samples were centrifuged at 1600*g* relative centrifugal force for 2 min (ROTOFIX 32 A, Andreas Hettich GmbH & Co. KG, Tuttlingen, Germany) to remove residual saline, completely for CELT^{plus} and partially for nanofat preparation. To ensure comparability, all processing steps followed the CELT protocol (*3*), except for mechanical emulsification. For CELT^{plus}, the lipoaspirate was passed five times between two 10-ml syringes through a 2.1-mm connector and then five additional times through a 1.0-mm constriction. For nanofat processing, less force and a wider connector (2.1 to ~1.5 mm) were used. All samples were recentrifuged under identical conditions. In CELT^{plus} samples, a distinct oil phase (>50% of the total volume) was removed postcentrifugation. In nanofat samples, no separable oil phase was observed, and the entire volume was retained.

Supplementary Materials

This PDF file includes:

Figs. S1 to S5

REFERENCES AND NOTES

1. A. Sambri, E. Caldari, M. Fiore, R. Zucchini, C. Giannini, M. G. Pirini, P. Spinnato, A. Cappelli, D. M. Donati, M. De Paolis, Margin assessment in soft tissue sarcomas: Review of the literature. *Cancers (Basel)* **13**, 1687 (2021).
2. H. A. Alturkistani, F. M. Tashkandi, Z. M. Mohammedsaleh, Histological stains: A literature review and case study. *Glob. J. Health Sci.* **8**, 72–79 (2015).
3. L. Prantl, A. Eigenberger, R. Reinhard, A. Siegmund, K. Heumann, O. Felthaus, Cell-enriched lipotransfer (CELT) improves tissue regeneration and rejuvenation without substantial manipulation of the adipose tissue graft. *Cells* **11**, 3159 (2022).
4. F. J. Voskuil, J. Vonk, B. van der Vegt, S. Kruijff, V. Ntziachristos, P. J. van der Zaag, M. J. H. Witjes, G. M. van Dam, Intraoperative imaging in pathology-assisted surgery. *Nat. Biomed. Eng.* **6**, 503–514 (2022).
5. D. Pertzborn, H.-N. Nguyen, K. Hüttmann, J. Prengel, G. Ernst, O. Guntinas-Lichius, F. von Eggeling, F. Hoffmann, Intraoperative assessment of tumor margins in tissue sections with hyperspectral imaging and machine learning. *Cancers (Basel)* **15**, 213 (2022).
6. R. Cao, S. D. Nelson, S. Davis, Y. Liang, Y. Luo, Y. Zhang, B. Crawford, L. V. Wang, Label-free intraoperative histology of bone tissue via deep-learning-assisted ultraviolet photoacoustic microscopy. *Nat. Biomed. Eng.* **7**, 124–134 (2023).
7. J. W. Baik, H. Kim, M. Son, J. Choi, K. G. Kim, J. H. Baek, Y. H. Park, J. An, H. Y. Choi, S. Y. Ryu, J. Y. Kim, K. Byun, C. Kim, Intraoperative label-free photoacoustic histopathology of clinical specimens. *Laser Photonics Rev.* **15**, 2100124 (2021).
8. S. Jeon, J. Kim, D. Lee, J. W. Baik, C. Kim, Review on practical photoacoustic microscopy. *Photoacoustics* **15**, 100141 (2019).
9. Z. Liu, L. Chen, H. Cheng, J. Ao, J. Xiong, X. Liu, Y. Chen, Y. Mao, M. Ji, Virtual formalin-fixed and paraffin-embedded staining of fresh brain tissue via stimulated Raman CycleGAN model. *Sci. Adv.* **10**, eadn3426 (2024).
10. X. L. Deán-Ben, H. López-Schier, D. Razansky, Optoacoustic micro-tomography at 100 volumes per second. *Sci. Rep.* **7**, 6850 (2017).
11. L. Wang, K. Maslov, J. Yao, B. Rao, L. V. Wang, Fast voice-coil scanning optical-resolution photoacoustic microscopy. *Opt. Lett.* **36**, 139–141 (2011).
12. M. Chen, X. Duan, B. Lan, T. Vu, X. Zhu, Q. Rong, W. Yang, U. Hoffmann, J. Zou, J. Yao, High-speed functional photoacoustic microscopy using a water-immersible two-axis torsion-bending scanner. *Photoacoustics* **24**, 100309 (2021).

13. J. Y. Kim, C. Lee, K. Park, G. Lim, C. Kim, Fast optical-resolution photoacoustic microscopy using a 2-axis water-proofing MEMS scanner. *Sci. Rep.* **5**, 7932 (2015).
14. J. Chen, Y. Zhang, L. He, Y. Liang, L. Wang, Wide-field polygon-scanning photoacoustic microscopy of oxygen saturation at 1-MHz A-line rate. *Photoacoustics* **20**, 100195 (2020).
15. J. Y. Kim, C. Lee, K. Park, S. Han, C. Kim, High-speed and high-SNR photoacoustic microscopy based on a galvanometer mirror in non-conducting liquid. *Sci. Rep.* **6**, 34803 (2016).
16. M. A. Pleitez, A. A. Khan, A. Soldà, A. Chmyrov, J. Reber, F. Gasparin, M. R. Seeger, B. Schätz, S. Herzig, M. Scheideler, V. Ntziachristos, Label-free metabolic imaging by mid-infrared optoacoustic microscopy in living cells. *Nat. Biotechnol.* **38**, 293–296 (2020).
17. B. Zhang, M. Sun, Y. Yang, L. Chen, X. Zou, T. Yang, Y. Hua, M. Ji, Rapid, large-scale stimulated Raman histology with strip mosaicing and dual-phase detection. *Biomed. Opt. Express* **9**, 2604–2613 (2018).
18. N. Davoudi, X. L. Deán-Ben, D. Razansky, Deep learning optoacoustic tomography with sparse data. *Nat. Mach. Intell.* **1**, 453–460 (2019).
19. J. Zhou, D. He, X. Shang, Z. Guo, S.-L. Chen, J. Luo, Photoacoustic microscopy with sparse data by convolutional neural networks. *Photoacoustics* **22**, 100242 (2021).
20. A. DiSpirito III, D. Li, T. Vu, M. Chen, D. Zhang, J. Luo, R. Horstmeyer, J. Yao, Reconstructing undersampled photoacoustic microscopy images using deep learning. *IEEE Trans. Med. Imaging* **40**, 562–570 (2021).
21. T. Vu, A. DiSpirito III, D. Li, Z. Wang, X. Zhu, M. Chen, L. Jiang, D. Zhang, J. Luo, Y. S. Zhang, Q. Zhou, R. Horstmeyer, J. Yao, Deep image prior for undersampling high-speed photoacoustic microscopy. *Photoacoustics* **22**, 100266 (2021).
22. D. He, J. Zhou, X. Shang, X. Tang, J. Luo, S.-L. Chen, De-noising of photoacoustic microscopy images by attentive generative adversarial network. *IEEE Trans. Med. Imaging* **42**, 1349–1362 (2023).
23. S. Siregar, R. Nagaoka, I. U. Haq, Y. Saijo, Non local means denoising in photoacoustic imaging. *Jpn. J. Appl. Phys.* **57**, 07LB06 (2018).
24. D. Allman, A. Reiter, M. A. L. Bell, Photoacoustic source detection and reflection artifact removal enabled by deep learning. *IEEE Trans. Med. Imaging* **37**, 1464–1477 (2018).
25. A. Hariri, K. Alipour, Y. Mantri, J. P. Schulze, J. V. Jokerst, Deep learning improves contrast in low-fluence photoacoustic imaging. *Biomed. Opt. Express* **11**, 3360–3373 (2020).
26. C. Bouchard, T. Wiesner, A. Deschênes, A. Bilodeau, B. Turcotte, C. Gagné, F. Lavoie-Cardinal, Resolution enhancement with a task-assisted GAN to guide optical nanoscopy image analysis and acquisition. *Nat. Mach. Intell.* **5**, 830–844 (2023).
27. Q. Yang, P. Yan, Y. Zhang, H. Yu, Y. Shi, X. Mou, M. K. Kalra, Y. Zhang, L. Sun, G. Wang, Low-dose CT image denoising using a generative adversarial network with Wasserstein distance and perceptual loss. *IEEE Trans. Med. Imaging* **37**, 1348–1357 (2018).
28. D. Mishra, S. Chaudhury, M. Sarkar, A. S. Soin, Ultrasound image enhancement using structure oriented adversarial network. *IEEE Signal Process Lett.* **25**, 1349–1353 (2018).
29. K. Suzuki, Overview of deep learning in medical imaging. *Radiol. Phys. Technol.* **10**, 257–273 (2017).
30. D. L. Donoho, Compressed sensing. *IEEE Trans. Inf. Theory* **52**, 1289–1306 (2006).
31. M. Haltmeier, T. Berer, S. Moon, P. Burgholzer, Compressed sensing and sparsity in photoacoustic tomography. *J. Opt.* **18**, 114004 (2016).
32. A. Béché, B. Goris, B. Freitag, J. Verbeeck, "Compressed sensing for beam sensitive materials imaging in Scanning Transmission Electron Microscopy" in *European Microscopy Congress 2016: Proceedings* (Wiley, 2016); https://doi.org/10.1002/9783527808465.emc2016.6174.
33. H. S. Anderson, J. Ilic-Helms, B. Rohrer, J. Wheeler, K. Larson, "Sparse Imaging for Fast Electron Microscopy" in *Computational Imaging XI*, C. A. Bouman, I. Pollak, P. J. Wolfe, Eds. (SPIE, 2013) vol. 8657, pp. 86570C.
34. E. Ortega, D. Nicholls, N. D. Browning, N. de Jonge, High temporal-resolution scanning transmission electron microscopy using sparse-serpentine scan pathways. *Sci. Rep.* **11**, 22722 (2021).
35. F. Ju, Y. Sun, J. Gao, Y. Hu, B. Yin, Nonparametric tensor dictionary learning with beta process priors. *Neurocomputing* **218**, 120–130 (2016).
36. E. Monier, T. Oberlin, N. Brun, X. Li, M. Tencé, N. Dobigeon, Fast reconstruction of atomic-scale STEM-EELS images from sparse sampling. *Ultramicroscopy* **215**, 112993 (2020).
37. V. V. T. Tran, K. Y. Hong, X. Jin, H. Chang, Histological comparison of nanofat and lipoconcentrate: Enhanced effects of lipoconcentrate on adipogenesis and angiogenesis. *Aesthetic Plast. Surg.* **48**, 752–763 (2024).
38. J. Knollmüller, T. A. Enßlin, Metric Gaussian variational inference. arXiv: 1901.11033 (2019).
39. I. Nseir, F. Delaunay, C. Latrobe, A. Bonmarchand, D. Coquerel-Beghin, I. Auquit-Auckbur, Use of adipose tissue and stromal vascular fraction in hand surgery. *Orthop. Traumatol. Surg. Res.* **103**, 927–932 (2017).
40. A. Eigenberger, O. Felthaus, T. Schratzenstaller, S. Haerteis, K. Utpatel, L. Prantl, The effects of shear force-based processing of lipoaspirates on white adipose tissue and the differentiation potential of adipose derived stem cells. *Cells* **11**, 2543 (2022).
41. M. Selig, M. R. Bell, H. Junklewitz, N. Oppermann, M. Reinecke, M. Greiner, C. Pachajoa, T. A. Enßlin, NIFTY – Numerical Information Field Theory. *Astron Astrophys* **554**, A26 (2013).
42. T. Steininger, J. Dixit, P. Frank, M. Greiner, S. Hutschenreuter, J. Knollmüller, R. Leike, N. Porqueres, D. Pumpe, M. Reinecke, M. Šraml, C. Varady, T. Enßlin, NIFTy 3 - Numerical Information Field Theory - A Python framework for multicomponent signal inference on HPC clusters. arXiv: 1708.01073 (2017).
43. J. Knollmüller, T. A. Enßlin, Encoding prior knowledge in the structure of the likelihood. arXiv: 1812.04403 (2018).

Acknowledgments: We thank M. C. Goess for providing adipose tissue samples for the validation study. Furthermore, we thank S. Lee for attentive reading and improvements of the manuscript. **Funding:** C.B., M.K., and M.A.P. received funding from the Deutsche Forschungsgemeinschaft (DFG) - 455422993 as part of the Research Unit FOR 5298 (iMAGO, subproject TP3, GZ: PL825/3-1). L.S.-P. and D.J. received funding from the European Research Council (ERC) under the European Union's Horizon Europe research and innovation program under grant agreement no. 101041936 (EchoLux). The development of the microscopy system has received funding from the DFG, Germany (Gottfried Wilhelm Leibniz Prize 2013; NT 3/10-1), as well as from the ERC under the European Union's Horizon 2020 research and innovation program under grant agreement no. 694968 (PREMSOT). **Author contributions:** Conceptualization: C.B., L.S.-P., D.J., M.A.P., and V.N. Formal analysis: C.B. Funding acquisition: V.N., D.J., and M.A.P. Investigation: C.B. and M.K. Methodology: C.B. and L.S.-P. Project administration: C.B. and M.A.P. Software: C.B. and L.S.-P. Resources: A.E., L.P., P.L., V.G., V.N., and M.A.P. Supervision: D.J. and M.A.P. Validation: C.B., M.K., and L.S.-P. Visualization: C.B., D.J., and M.A.P. Writing—original draft: C.B., M.K., L.S.-P., A.E., P.L., and M.A.P. Writing—review and editing: C.B., M.K., L.S.-P., L.P., V.G., D.J., and M.A.P. **Competing interests:** V.N. and M.A.P. are founders and equity owners of sThesis GmbH. V.N. is a founder and equity owner of Maurus OY, iThera Medical GmbH, Spear UG, and I3 Inc. A patent application (WO 2019 149 744 A1) licensed to sThesis GmbH, relevant to the technology discussed in this paper, has been filed. The other authors declare that they have no competing interests. **Data and materials availability:** The source code for image reconstruction used for BayROM was published along with an example image on Zenodo (https://doi.org/10.5281/zenodo.15222977). All data needed to evaluate the conclusions in the paper are present in the paper and/or the Supplementary Materials.

Submitted 19 November 2024
Accepted 22 July 2025
Published 22 August 2025
10.1126/sciadv.adu7319